Higher order ferromagnetic resonances in out-of-plane saturated magnetic multilayers

Fallarino, L.; Stienen, S.; Gallardo, R. A.; Arregi, J. A.; Uhlíř, V.; Lenz, K.; Hübner, R.; Oelschlägel, A.; Hellwig, O.; Lindner, J.;

Originally published:

September 2020

Physical Review B 102(2020), 094434

DOI: https://doi.org/10.1103/PhysRevB.102.094434

Higher order ferromagnetic resonances in out-of-plane saturated magnetic multilayers

L. Fallarino,[1] S. Stienen,[1] R. A. Gallardo,[2,3] J. A. Arregi,[4] V. Uhlíř,[4,5] K. Lenz,[1] R. Hübner[1], O. Hellwig,[1,6] and J. Lindner[1]

[1]Helmholtz-Zentrum Dresden-Rossendorf, Institute of Ion Beam Physics and Materials Research, Bautzner Landstrasse 400, 01328 Dresden, Germany.

[2]Departamento de Física, Universidad Técnica Federico Santa María, Avenida España 1680, 2390123 Valparaíso, Chile

[3]Center for the Development of Nanoscience and Nanotechnology (CEDENNA), 917-0124 Santiago, Chile

[4]CEITEC BUT, Brno University of Technology, Purkyňova 123, 612 00 Brno, Czechia.

[5]Institute of Physical Engineering, Brno University of Technology, Technická 2, 61669 Brno, Czechia

[6]Institute of Physics, Chemnitz University of Technology, D-09107 Chemnitz, Germany.

Abstract

Artificial ferromagnetic (FM)/nonmagnetic multilayers, with large enough FM thickness to prevent the dominance of interface anisotropies, offer a straightforward insight into the understanding and control of perpendicular standing spin wave (PSSW) modes. Here we present a study of the static and dynamic magnetic properties of $[\mathrm{Co}(3.0\,\mathrm{nm})/\mathrm{Au}(0.6\,\mathrm{nm})]_{1\leq N\leq 30}$ multilayer systems. Magnetometry reveals that the samples exhibit magnetization reversal properties typical of an effective single layer with weak perpendicular anisotropy, with the distinctive thickness-dependent magnetization reorientation transition from in-plane to out-of-plane. When such multilayer systems are out-of-plane saturated however, the dynamic response reveals the existence of several different ferromagnetic resonances in the form of PSSW modes that strongly depend on the material modulation characteristics along the total thickness. These modes are induced by the layer stacking itself as the effective single layer model fails to describe the complex dynamics observed in the system. In contrast to most systems considered in the past, described by a dynamic model of a single effectively homogeneous thick layer, the specific structures investigated here provide a unique platform for a large degree of tunability of the mode frequencies and amplitude profiles. We argue that the combination of periodic magnetic properties with vertical deformation gradients, arising from heteroepitaxial strain relaxation, generates a vertical regular array of two-dimensional pinning sites for the PSSW modes, which promotes the complex dynamics observed in the system.

I. Introduction

Multilayer (ML) systems consisting of alternating layers of ferromagnetic (FM) and non-magnetic (NM) materials have gained steadily growing interest from fundamental physical perspective as well as for technological applications [1-3]. Due to the large variety of short- and long-range interactions acting in these MLs, their characteristics can be conveniently modified through small changes in the specifics of the layer stack. Concerning the static magnetic behavior, the uniform out-of-plane (OOP) magnetic ground state may be achieved by appropriately choosing the material parameters, primarily supported by the FM/NM interfaces (surfaces) in the thin film regime [4-7]. An increase of either the thickness of the individual FM layer component or the total number of the FM/NM repetitions causes the occurrence of non-uniform microscopic magnetization states, resulting in a magnetization reversal process dominated by the collective propagation of OOP domains [8-10]. However, this change could also lead to a complete in-plane (IP) reorientation of magnetization. This may be due to either the absence of a sufficiently high OOP magneto-crystalline anisotropy or an insufficient ML volume, both causing an IP uniform state being preferred over an OOP domain state [11-16]. Indeed, these changes do not only impact the static magnetic properties, but substantially also the dynamic behavior of ML systems.

Out of many experimental methods that have been applied to dynamic studies, ferromagnetic resonance (FMR) has proven to be one of the most powerful tools to sensitively evaluate any change and evolution of magnetic properties [17-22]. While measuring the uniform or quasi-uniform resonant mode, information about the volume averaged magnetic properties can be gained. The higher order modes are more sensitive instead to exchange and anisotropy energies spatially varying across the thickness as well as to OOP magnetic inhomogeneities or modulations within the system [17-23]. Among the latter, perpendicular standing spin wave (PSSW) modes are excitations confined within the thickness of the film. Their wavelengths are usually determined by the total thickness and the magnetization pinning conditions at the top/bottom surfaces, which also govern the energy needed to access and drive the PSSW modes in FM single layers [23-27]. Although PSSW modes have been already investigated in homogeneous thick films as well as in ML systems to quite some extent, their behavior in FM/NM-systems in the regime of thick individual FM-layers—too thick to allow the interface anisotropy to dominate—has not been studied so far. In fact, FM/NM multilayers naturally provide a suitable platform to introduce systematic and regular layer-like pinning sites at the interfaces throughout the total thickness, otherwise confined at the top and bottom surfaces of a magnetically homogeneous system. Therefore, MLs represent an efficient means to excite and manipulate such exchange-dominated spin-wave modes, which could potentially have implications for novel high-frequency spintronic applications [27-29].

The studied system consists of $[\mathrm{Co}(3.0\ \mathrm{nm})/\mathrm{Au}(0.6\ \mathrm{nm})]_N$ MLs with a variable number of Co/Au bilayer *N*. We have chosen the individual and total thicknesses such that the interface-induced anisotropy is not primarily driving the static magnetic response. Moreover, we have grown our ML structures on top of a thick Au(111) buffer layer, such that Co, which adopts at room temperature the hexagonal close-packed (*hcp*) crystal structure and exhibits a magnetic easy axis along the *hcp* crystal *c*-axis, grows with the necessary crystallographic texture to induce an OOP anisotropy-axis orientation supported by the specific total thickness range [11,14-16,30]. We note that similar multilayer sample structures, where the Au(0.6 nm) layers were substituted by Pt(0.6 nm) layers, were already fully statically characterized [30] and provided valuable knowledge for the dynamic studies presented here. Finally, the proposed FMR model is based on the Landau-Lifshitz equation of motion [31] in order to explain the experimental data, where variations of the anisotropy fields along the thickness of the ML structure are included.

The paper is organized as follows. We describe the experimental details in Sec. II. Then, Sec. III A details the identification of the crystal structure and the evaluation of the epitaxial relationships. In Sec. III B, the room-temperature magnetometry characterization is presented, whereas the FMR spectroscopy study together with analytical calculations are discussed in Sec. III C. Finally, Sec. IV provides a summary of the results and general conclusions.

II. Experimental details

The samples were grown at room temperature by dc magnetron sputtering in an ultrahigh vacuum system (ATC 2200 series from AJA International, Inc.) with a base pressure better than 3×10^{-6} Pa. Si(001) substrates covered by a 100-nm-thick thermal SiO_x layer were used. Each layer was deposited using a pure Ar pressure of 4×10^{-1} Pa. The $[\mathrm{Co}(3.0\ \mathrm{nm})/\mathrm{Au}(0.6\ \mathrm{nm})]_N$ MLs were grown on Ta(1.5 nm)/Au(20 nm) seed layers. The Au (20 nm) buffer layer serves to maximize the *hcp* (0001) texture within the Co/Au MLs similar as also done with Pt seed layers in Co/Pt multilayers [30]. The thickness of the Au cap layer was 2.4 nm, which is sufficient to prevent oxidation as well as aging effects after removal from the vacuum system. Au as capping material has also been chosen to avoid breaking the spatial inversion symmetry along the OOP direction of the ML [32]. The investigated periods of the ML were N = 1, 2, 3, 4, 6, 8, 10, 14, 18, 22, 26, and 30. A schematic representation of the sample structure, including its specific layer sequence and thicknesses, is shown in Fig. 1. The structural analysis of the samples was performed by means of x-ray diffraction (XRD) and reflectivity (XRR) utilizing a Rigaku SmartLab X-ray thin film diffractometer operated with Cu-K_α radiation. Magnetization measurements were performed using a Microsense EZ7 vibrating sample magnetometer (VSM), equipped with a 360° rotational stage. The dynamic magnetic properties were characterized by means of vector network analyzer ferromagnetic resonance spectroscopy (VNA-FMR). The samples were placed flip-chip onto a coplanar waveguide and the complex transmission parameter S_{21} was measured at constant frequency as the FMR signal, while the magnetic field was swept through resonance [33,34].

III. Results and Discussion

A. Structural characterization

Figure 1 illustrates XRR scans in the range of $0.5° \leq 2\theta \leq 8.0°$ for the entire set of Co/Au samples, with the left inset showing the specific layer sequence that we used including all template layers.

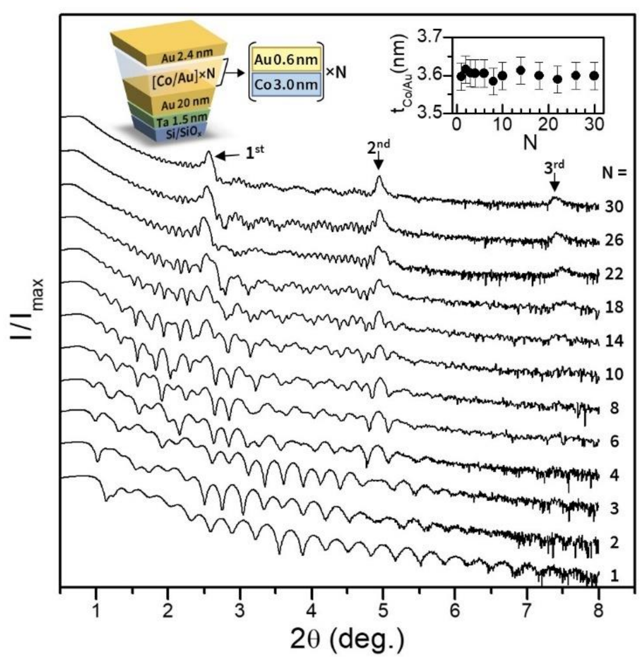

FIG. 1. XRR scans of all $[Co(3.0nm)/Au(0.6nm)]_N$ multilayer samples with $1 \leq N \leq 30$ repetitions. The top-left inset shows a schematic drawing of the layer stack. The top-right inset displays the average total thickness of the single Co/Au bilayer as a function of N as obtained from XRR measurements.

Interference-caused Kiessig fringes with two different periods are distinguishable in Fig. 1 for high N. The first type with a period inversely proportional to N can be observed at low 2θ values. These short-period oscillations correspond to the total thickness of the MLs, since by increasing N (i.e. the total sample thickness) the distance between two consecutive minima or maxima decreases. At the same time their relative intensity decreases while increasing N, due to the increasing number of interfaces as well as due to the light absorption in each individual layer. In a wider 2θ-range a second set of Kiessig fringes is noticeable, whose period ($\Delta\theta \approx 0.2°$) is constant as a function of N. They originate from the 20-nm-thick Au buffer layer. More importantly, the development of first, second, and third order Bragg-like superstructure peaks are observed with increasing N, giving a clear signature of a well-defined periodic elemental ML modulation. Fitting them to a Gaussian profile, the total thickness of the repeating Co/Au bilayer $t_{Co/Au}$ was evaluated [35]. The right inset in Fig. 1 shows the N-dependence of $t_{Co/Au}$, where the error bars correspond to the standard deviation values. Under the assumption of a purely statistical Gaussian distribution for the observed $t_{Co/Au}$ values, the data sets fall into the interval defined by $t_{co/Au} = 3.61 \pm 0.02$ nm, consistent with the nominal Co/Au bilayer thickness of 3.6 nm.

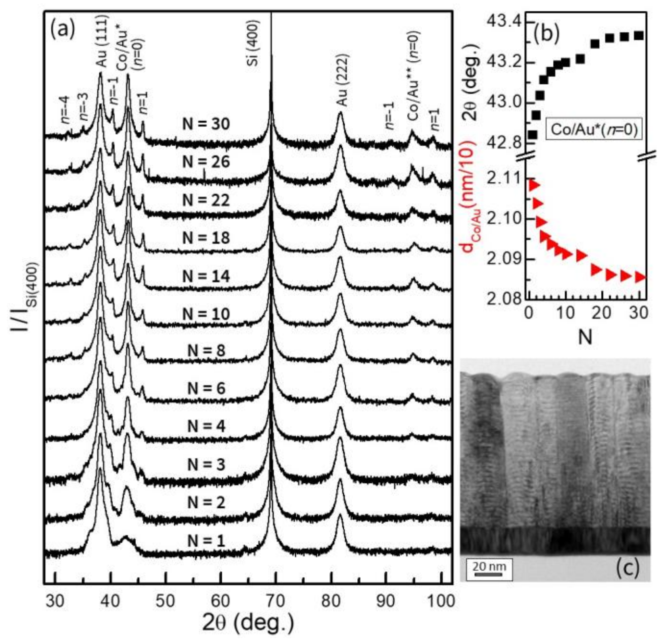

FIG. 2. (a) X-ray θ-2θ scans of all samples. Each scan has been normalized to the intensity of its Si (400) substrate peak. (b) The top panel shows the N dependence of the Co/Au* (n=0) diffraction peak position (squares), while the bottom panel displays the associated average out-of-plane interplanar distance $d_{Co/Au}$ of the Co/Au heterostructure vs. N. (c) Cross-sectional TEM image of the [Co(3.0 nm)/Au(0.6 nm)]$_{30}$ sample.

Figure 2(a) shows the XRD scans in the full angular range $28° \leq 2\theta \leq 102°$ for all Co/Au samples. All the scans look very similar in their overall appearance, exhibiting only well-defined diffraction peaks corresponding to Si(004), Au(111), and Au(222) originating from the buffer layer. The superstructure reflections Co(0002)/Au(111) and Co(0004)/Au(222) are visible as well.

In the following they are abbreviated as Co/Au* and Co/Au** respectively. Even though heteroepitaxial growth of crystalline layers is usually performed directly on top and facilitated by single crystalline substrates, the presence of a thermally oxidized SiO_x thick layer is not preventing the sputtered Au thin films from developing a highly oriented *fcc* (111) textured growth [30]. In fact, *fcc* metal films have the largest atomic packing density along the (111) crystal plane and thereby the lowest surface energy. Therefore, while using such materials as buffer layers, the sample architecture studied in this work could very well be transferred to a large variety of different substrates without losing the specific crystal quality. Moreover, the Au buffer layer peaks look virtually the same for all samples, both in terms of angular position and peak width, verifying the robustness of our fabrication process.

Hereby, the total X-ray scan angular range shows only well-defined *fcc*(*nnn*) and *hcp*(0002*l*) peaks for Au and Co, respectively [36]. Moreover, satellite reflections around the superstructure diffraction peaks [indexed by n in Fig. 2(a)] have been measured, which are a clear indication of a perpendicular structural coherence length far larger than the thickness of the individual constituent layers. It can be also observed that the negative indexed satellite diffraction peaks for the Co/Au samples have higher intensity than the positive ones, with the latter being within the noise level for $n > 1$. This effect, whose prominence being mainly appreciable for the first order diffraction peaks, is mainly caused by the overlapping and interfering waves coming from the negatively indexed satellite diffractions and the Au(111) reflection.

Furthermore, the diffraction conditions for the Au(111) lattice planes occur at different angles, due to their different lattice dimensions resulting in $d_{111,\mathrm{Au}} = 0.236$ nm, compared to the volume-averaged Co(3.0nm)/Au(0.6nm) bilayer, corresponding to $d_{\mathrm{Co/Au*}} = 0.208$ nm. This would lead to different magnitudes of strain throughout the ML structures depending on the number of times the Co/Au bilayer building block was repeated. Thus, one could anticipate that otherwise identically prepared and similar films of different thickness may have different depth-dependent strain profiles. As expected, the diffraction peak intensity for Co/Au* and Co/Au** increases as the total structure becomes thicker, simply due to the larger amount of epitaxially ordered material. Nevertheless, upon carefully analyzing their angular position as a function of N [Fig.2(b)], a continuous shift to higher 2θ angles is found as N increases. This indicates that for small N the Co/Au bilayers are under larger tensile strain, which is partially being released as the growth progresses. For samples with a larger value of N, the thickness dependent strain relaxation becomes increasingly prominent, hereby approaching a bulk-like lattice parameter value as shown in Fig.

2(b). This process is occurring within each sample via the internal relaxation of the lattice mismatch induced stress by the occurrence of misfit dislocations and lattice defects during growth, which would then propagate towards the Co/Au interfaces. One could also conclude that the dislocations are more numerous in the early stages of growth once they start to form, as the stress needed to relief is larger at this point as compared to the topmost extent of the larger *N* samples, where a significant part of the stress has already been released. From this point of view, it is reasonable to assume that the Co/Au ML samples possess a gradient of strain across their vertical extent. In spite of these considerations, the first and second order superstructure diffraction peaks for the Co/Au MLs occur at nearly the same angle for $N > 10$ repetitions, thus indicating that the total thickness is larger than the critical thickness needed to relax the corresponding strains.

Moreover, it cannot be neglected that the presence of several interfaces due to the alternate deposition of FM/NM layers could influence the ML growth by inducing the formation of specific morphological features. Fig. 2(c) shows a cross sectional bright-field TEM image for $N = 30$. Without impacting the detectable and well-defined crystallographic texture measured using X-rays, a columnar structure is clearly visible in the micrographs together with a precise and well-established layered structure. The columns are mostly extended throughout the whole thickness of the ML film and are largely perpendicular to the substrate with almost parallel walls. Nonetheless, cumulative layer waviness is also observed due to the shadowing effects inherent to the room temperature sputtering process and as a result of the heteroepitaxial growth initiated from the buffer layer and followed by two distinct material species with different epitaxial relationships, as well as due to the thickness discrepancy of the constituent layers in the ML [37,38]. Thus, both the observed strain-relaxation and waviness can be regarded as important aspects related to the magneto-dynamic properties of our samples, as will be discussed in Section IIIC. Hereby, our structural analysis confirms the good crystallographic quality of the optimized layer growth sequence resulting in well-modulated Co/Au MLs with perpendicular c-axis orientation, necessary for a preferential OOP orientation of the magnetization above a critical thickness [11-16].

B. Magnetostatic characterization

Figures 3(a)-(l) present room temperature normalized M/M_S data as a function of the field strength $\mu_0 H$ and number of Co/Au bilayer repetitions *N*, with M_S being the saturation magnetization. In each graph, the (black) short dashed and (red) solid lines show the magnetization reversal curves measured for an external magnetic field applied parallel and perpendicular to the film plane, respectively. Each sample with $14 \leq N \leq 30$ shows two reversal curves that are a clear indication of an OOP preferential orientation of magnetization [8,14,16,30].

For the IP field configuration, as one lowers the applied magnetic field, the saturated state becomes unstable at a critical field H_{cr} [pointed to in Fig.3(l)] and undergoes laterally alternating magnetization rotations into a tilted stripe domain state driven by the magnetocrystalline OOP anisotropy [8,14,16,30]. For $0 < H < H_{cr}$ this tilted stripe domain state becomes the system ground state [39] and the precursor to perpendicular stripe domains at remanence. Its OOP magnetization modulation increases, and the IP magnetization decreases as the applied field is further reduced, which leads to the overall curved appearance of all the in-plane $M(H)$ measurements in Fig. 3 for $14 \leq N \leq 30$. However, a final IP magnetization component still persists at remanence due to Bloch type domain walls that have been aligned during the field sequence into the in-plane external field direction and that are responsible for the IP hysteresis that occurs for low field values [14-16].

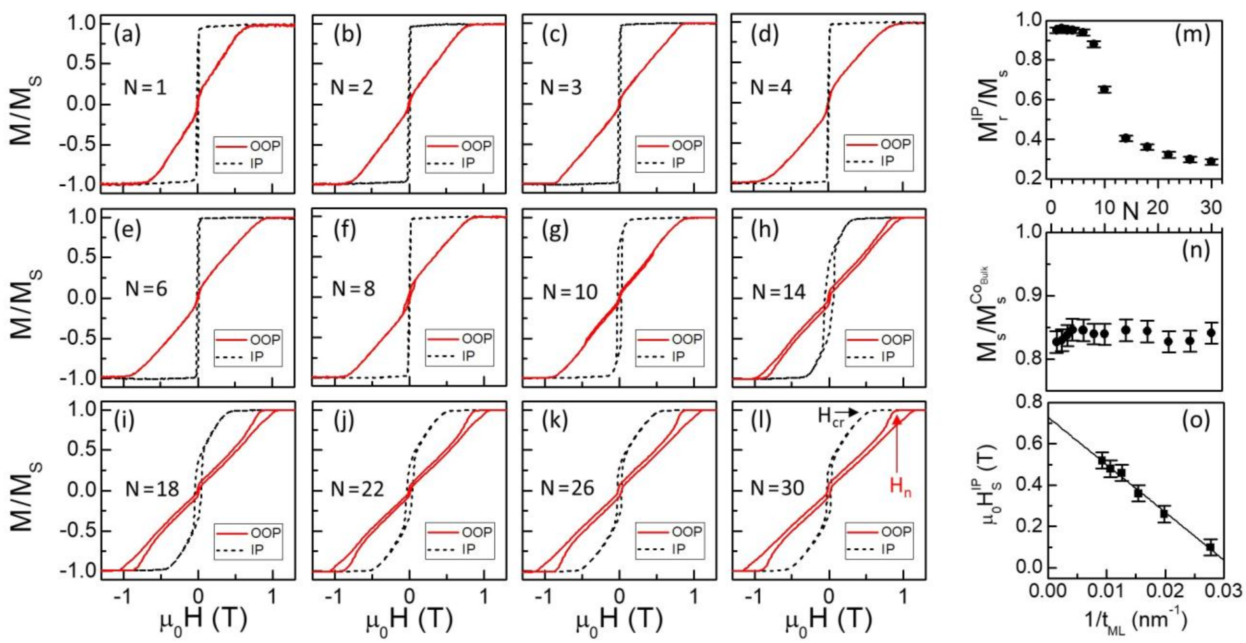

FIG. 3. (a)-(l) VSM room temperature (RT) magnetization reversal curves with the applied field along the IP (black dashed lines) and OOP (red full lines) directions for the entire set of $[Co(3.0\ nm)/Au(0.6\ nm)]_N$ samples. Data is normalized to its M_S in each case. (m) N-dependence of the in-plane remanence ratio M_r^{IP}/M_S [obtained from the magnetometry data of (a)-(l)]. (n) RT saturation magnetization M_S as a function of the Co/Au bilayer repetitions N. (o) RT in-plane saturation field $\mu_0 H_s^{IP}$ as a function of the inverse total multilayer thickness $t_{ML} = N \times \Lambda$, with $\Lambda = 3.6$ nm being the Co/Au bilayer period. The solid line represents the least-squares fits to Eq. (1).

For the OOP field configuration instead, once the field is lowered, the uniform state is broken by the formation of bubble domains with opposite OOP magnetization orientation driven by magnetostatic energy. This process starts rather abruptly at the nucleation field H_n^{OOP} [pointed out in Fig. 3(l)], leading to a sharp drop in the magnetization. As the field is further reduced the domain dimensions increase to minimize the total magnetostatic energy resulting in the linear field dependence of the magnetization down to remanence [9,40,41]. Finally, the small hysteresis effect is the result of a non-uniform domain expansion and contraction, which is related to the existence of slight sample imperfections. An appreciable change is noticeable as well in the two OOP-hysteretic regions at high field magnitudes, associated with the initial nucleation and final annihilation of domains. In fact, upon increasing N, i.e. the total thickness, their position along the magnetic field axis shifts to progressively higher values as well as their hysteretic area becomes gradually larger [14-16,30].

For the samples with $1 \leq N \leq 8$, despite the OOP orientation of the magnetocrystalline anisotropy axis, an IP behavior was found. For those samples the measurements show almost perfectly rectangular-shaped hysteresis loops for the IP applied field. In contrast, the OOP field data in Figs. 3(a)-(f) show an almost completely reversible change in the magnetization orientation where the complete alignment is reached only at a field strength of $\mu_0 H^{\mathrm{OOP}} \approx \pm 1$ T.

Figure 3(g) shows the IP and OOP magnetization curves for the sample with $N = 10$. While the OOP curve shows the absence of high field nucleation hysteresis near saturation, the IP configuration demonstrates the persistence of a strong curvature of the loop and a very small remanent magnetization. Thus, the sample is evidently not in an IP magnetization state at remanence, meaning that it must undergo a perpendicular or tilted stripe domain reversal process if one lowers the externally applied field [30].

Finally, from our experimental data in Fig. 3, we concluded that N has a profound impact on the magnetization reversal characteristics of $[\mathrm{Co(3nm)/Au(0.6nm)}]_N$ MLs. The overall appearance of the IP and OOP magnetization reversal curves stays very similar for $14 \leq N \leq 30$ [Figs. 3(h)–(l)]. However, while lowering the number of repetitions, thickness-induced magnetization reorientation transition takes place, which culminates with a reversal mechanism characterized by IP magnetization states alone [11,15,30]. The transition from a remanent OOP stripe domain state (for $N \geq 14$) to a remanent uniform in-plane state (for $N \leq 8$) is mainly driven by the canting of the local magnetization [30]. Such canting angle varies monotonically with N as indicated by the N dependence of the IP remanence ratio M_r^{IP}/M_S shown in Fig. 3(m). Samples with $N > 14$ exhibit a low M_r^{IP}, arising mainly from the local magnetic moments confined inside the domain walls. The IP remanence gradually increases when lowering N, indicating a canting of the domain magnetization towards the film plane. Finally, the ratio reaches values corresponding to a full IP remanent magnetization, thus confirming that the Co/Au samples (for $1 \leq N \leq 8$) are evidently in an IP-magnetized state at remanence.

The observed magnetic crossover from OOP to IP should be still correctly described by treating each ML as an effective single layer systems with the same saturation magnetization M_S, anisotropy K_u, and exchange stiffness A for each different total thickness [14,15,42-47]. We have determined the room temperature saturation magnetization M_S for the entire set of samples with different N by taking into account the total magnetic thickness as $t_{ML} = N \times \Lambda$, with $\Lambda = 3.6$ nm being the Co/Au bilayer period. The results are plotted in Fig. 3(n) after having them normalized to the bulk value of the Co saturation magnetization of 1450 kA/m [48]. The data are showing that the ratios are nearly independent of N, i.e. the total thickness, with an average value of $\overline{M_S(\mathrm{Co/Au})/\,M_S^{Co_{bulk}}} = 0.84 \pm 0.01$. The stability of M_S and other magnetic parameters (see below) allows us to ascribe any significant change in the magnetic properties to the specific number of repetitions N as opposed to the inherent Co thickness variations or substantial CoAu alloying, which would both lead to substantial variation in the saturation magnetization. However, we could see that by increasing N from 1 to 4, the volume-averaged saturation magnetization slightly increases. In an alloy material $FM_{1-x}NM_x$ the saturation magnetization monotonically decreases, while increasing the percentage of the NM element x. In our MLs the same effect is occurring at low N due to the very small magnetic moment induced into Au [49].

Furthermore, the invariance of effective single layer magnetic parameters while changing N [15,46], can be also verified by the linear relationship between the IP saturation field $\mu_0 H_s^{IP}$ and the inverse of the total ML thickness t_{ML}:

$$\mu_0 H_s^{IP} = \frac{2K_u}{M_S} - \frac{2K_u}{M_S}\frac{1}{\sqrt{1+\frac{2K_u}{M_S^2}}}\frac{t_{cr}}{t_{ML}} \tag{1}$$

with t_{cr} being the critical thickness at which the reorientation transition occurs. In Fig. 3(o) we show the $\mu_0 H_s^{IP}$ experimental data for $10 \leq N \leq 30$ as a function of $1/t_{ML}$, excluding the samples that show already a preferential IP magnetization. All the data follow a linear trend and share a common intercept $2K_u/\mu_0 M_s = 0.73$ T. Furthermore, we have obtained $t_{cr} = 41.4 \pm 1.8$ nm (approx. corresponding to $N = 12$), in agreement with the experimental data. It is worth emphasizing the point that the evaluated magnetic anisotropy is integrated over the entire ML volume, and thus, the total-thickness dependent (or stress release dependent) interface and magnetocrystalline anisotropies within each sample are averaged out.

Accordingly, despite the existence of a magnetization magnitude modulations along the thickness, whose degree depends on the nonmagnetic material, all the samples behave as single effective ferromagnetic layers with weak PMA under the application of external magnetic fields [14,16]. Nonetheless, all the OOP reversal curves are almost identical in the high field regime. Therefore, appreciable changes from sample to sample are not expected in terms of dynamic properties of their magnetization in the saturated state. However, and as already shown in Fig. 2 and discussed in Sec. IIIA, the interface and magnetocrystalline anisotropy should be considered as thickness dependent due to the strain evolution within each ML sample along the thickness, which will be the focus of the following Section.

C. *FMR study*

The FMR was measured using a VNA-based spectrometer in a field-sweep-mode. For each field-sweep a fixed microwave frequency in the range from 0 to 35 GHz was selected.

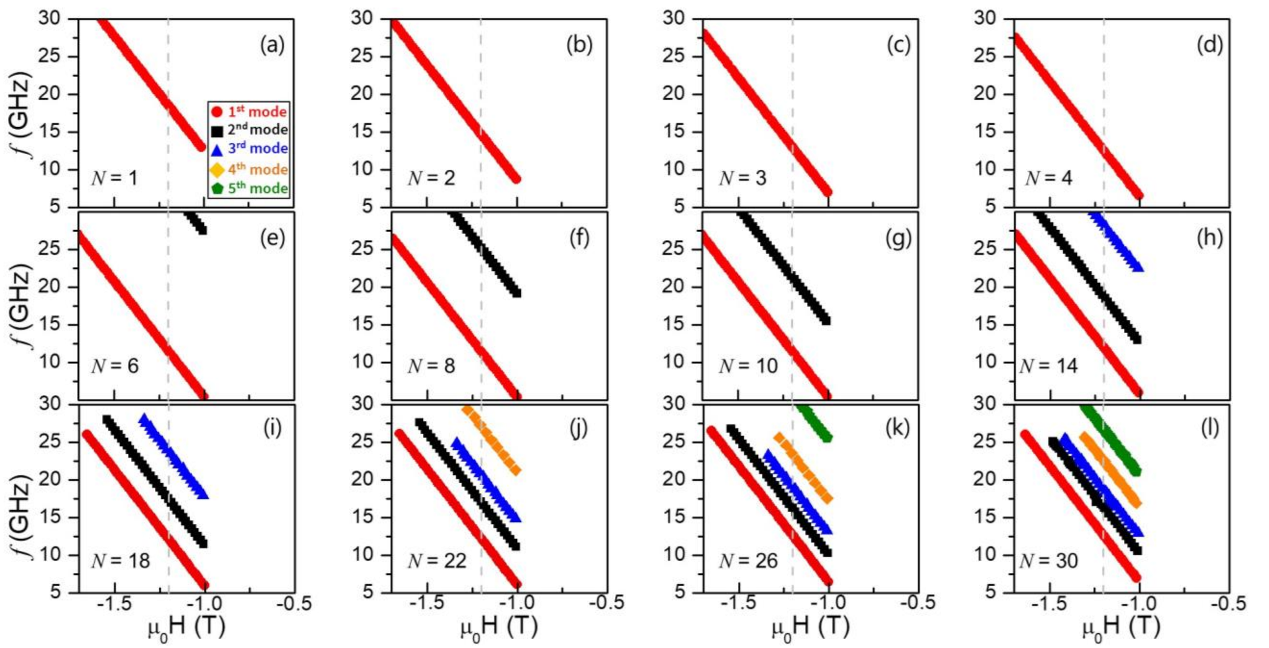

FIG. 4. (a)-(l) Frequency vs. field dependences of the ferromagnetic resonance for each sample. The external OOP field was always swept from -1.7 T to -1 T, ensuring always saturated OOP states. The vertical dashed (gray) lines mark the value $\mu_0 H$ = -1.2 T corresponding to the vertical cut that is used to construct Fig. 5.

As we have seen from the hysteresis curves in Fig. 3, a static OOP magnetic field of $\mu_0 H = \pm 1$ T is sufficient to saturate the magnetization of each sample in the normal direction. Therefore, to ensure that all measurements start and run in the same magnetic state, the magnetic field was always swept from $\mu_0 H$ = -1.7 T to $\mu_0 H$ = -1 T. The FMR spectra were fitted with a complex Lorentzian function to retrieve the resonance fields.

Figure 4 shows the resonance frequency as a function of the static external magnetic field for all samples (N) of our series. Figure 4(a) shows the data of the thinnest sample in this study, i.e., N = 1 or Au(20 nm)/Co(3 nm)/Au(3 nm). Only one mode is visible in the explored frequency range, which corresponds to the uniform magnetization precession mode in the single Co layer characterized by a uniform dynamic magnetization across its thickness. At the other end of our sample series, Fig. 4(l) displays the frequency-field dependence of the thickest N = 30 sample. In this case, many modes are visible. The modes are always labeled from bottom to top, i.e. from lowest frequency (1st mode, red dots) to highest frequency (5th mode, green pentagons). As mentioned above for a uniform single layer material, the detected FMR mode may be associated with the uniform precession of the magnetization. However, as we will see in detail further, the ML nature of the samples introduces a more complex scenario with a distribution of FMR amplitudes along the structure. The higher-order modes (2nd to 5th) can be identified as "PSSW-like" along the ML thickness. The observation of both odd and even modes implies that the mode amplitude profiles are asymmetric with respect to the sample thickness. Intriguingly, by decreasing the number of Co/Au repetitions from N = 30 backward, all the PSSW-like modes could still be excited at higher frequencies when the same static field is applied. Importantly, higher order modes have not been measured for $N < 6$. This might suggest an apparent suppression due to the thickness driven reorientation transition from OOP to IP preferential magnetization orientation. Contrary, the absence of the higher-order responses is associated to their shift in frequency into a range not accessible by our experimental setup (>35 GHz).

Moreover, the separation in frequency between the modes increases with decreasing the total ML thickness, which could be understood on the basis of the perpendicularly quantized spin wave vector being inversely proportional to the total film thickness. However, not only the PSSW-like modes are changing their resonance conditions upon changing N, but also the 1st mode. As already discussed in Sec. IIB, magnetometry has revealed a magnetic crossover from OOP to IP as a function of the total thickness, with the samples $N \geq 10$ being correctly described with the same values of saturation magnetization M_S, anisotropy K_u and exchange stiffness A. Nonetheless, those magnetic parameters were evaluated by an integral method (VSM) and XRD characterization has shown that the diffraction angle corresponding to the Co/Au superstructure Bragg peaks [displayed in Fig. 2(b)] shifts towards its bulk position with a steep increase between $1 \leq N \leq 10$. The angular position is directly related to the accommodation of misfits across any interface between Co and Au due to strain relaxation. This would correspond to an evolution of the interface quality as a function of N, which is dramatic for $N \leq 10$. This is therefore translated to the dynamic properties of such structures, as the 1st mode purely shows, given that it is not affected by total thickness effects. Indeed, for $N > 10$, a small change of the frequency positions of the FMR mode is still appreciable: despite corroborating that statically all these samples have the same structural properties and in particular the same Co and Au thicknesses, thus leading to nearly identical volume averaged magnetocrystalline and interface anisotropy fields, the dynamic response reveals the existence of small monotonic changes as N (and hence the total ML thickness) increases. We will argue that these changes originated in structural inhomogeneities (in particular, strain) along the vertical direction of the Co/Au ML stack.

In order to model the investigated samples from a dynamic point of view, a more detailed approach has been applied with respect to the single effective layer model, which was sufficient to understand the thickness-dependent magnetization reorientation transition but cannot explain the dynamic response. The model includes a bilinear interlayer exchange coupling throughout the Au interlayers [50,51]. Thus, the interaction between two consecutive Co layers ν and η is given by:

$$\epsilon_{\text{int}} = -J \frac{\mathbf{M}^{(\nu)} \cdot \mathbf{M}^{(\eta)}}{M_s^{(\nu)} M_s^{(\eta)}} \tag{2}$$

with J being the interlayer exchange constant. Although it is not necessary to understand the static properties of the investigated MLs, here the model includes surface anisotropies that are known to be induced by any Au/Co interface [52,53]. For the two outer Co layers (top-most and bottom-most) the effective anisotropy field is denoted by H_a^o, while H_a corresponds to the effective anisotropy field of the inner Co layers. Moreover, given that we are interested in the OOP saturated regime promoted by sufficient external magnetic field, we assume that the equilibrium magnetization of all layers is pointing along the normal axis. The time evolution of the magnetization is determined by the Landau–Lifshitz (LL) equation of motion [31], namely

$$\dot{\mathbf{M}}^{(\nu)}(\mathbf{r}, t) = -\mu_0 \gamma \mathbf{M}^{(\nu)}(\mathbf{r}, t) \times \mathbf{H}^{e(\nu)}(\mathbf{r}, t) \tag{3}$$

Here, the dot denotes the time derivative, γ is the absolute value of the gyromagnetic ratio, $\mathbf{M}^{(\nu)}(\mathbf{r}, t)$ is the magnetization, and $\mathbf{H}^{e(\nu)}(\mathbf{r}, t)$ is the effective field of the Co layer ν, respectively. In the linear approximation, both the magnetization and the effective field are written as

$\mathbf{M}^{(\nu)}(\mathbf{r},t) = M_s^{(\nu)}\hat{z} + \mathbf{m}^{(\nu)}(\mathbf{r},t)$ and $\mathbf{H}^{e(\nu)}(\mathbf{r},t) = \mathbf{H}^{e0(\nu)} + \mathbf{h}^{e(\nu)}(\mathbf{r},t)$. Note that the *z*-axis is aligned parallel to the normal axis, which corresponds to the equilibrium direction. In terms of the magnetization components, the LL equations of motion are

$$i\,\frac{\omega}{\mu_0\gamma} m_x^{(\nu)} = -m_y^{(\nu)} H_z^{e0(\nu)} + M_s^{(\nu)} h_y^{e(\nu)} \tag{4}$$

$$i\,\frac{\omega}{\mu_0\gamma} m_y^{(\nu)} = m_x^{(\nu)} H_z^{e0(\nu)} - M_s^{(\nu)} h_x^{e(\nu)} \tag{5}$$

where we assumed $\mathbf{m}^{(\nu)}(t) = \mathbf{m}^{(\nu)} e^{i\,\omega t}$ with $\omega = 2\pi f$, where f is the frequency. The spatial dependence of the magnetization has been omitted, since we are interested in the ferromagnetic resonance response, so that the wavelength of the spin waves is supposed to be very large and hence a coherent IP motion of the magnetic moments is expected in each Co layer. Now, the static *z*-component of the effective field is

$$H_z^{e0(\nu)} = H + H_a^{(\nu)} - M_s^{(\nu)} + \sum_\eta \left(d\mu_0 M_s^{(\nu)}\right)^{-1} J(\delta_{\nu-1}\delta_\eta + \delta_{\nu+1}\delta_\eta). \tag{6}$$

where H is the external field, $H_a^{(\nu)}$ is the effective anisotropy field (encompassing surface magnetic anisotropy and magnetocrystalline anisotropy contributions, $H_a^{(\nu)} = (H_K^{(\nu)} + H_S^{(\nu)})$, $M_s^{(\nu)}$ is the demagnetizing field of the uniform state, d is the thickness of the ν-th Co layer (3 nm) and $\delta_{i,j}$ is the Kronecker delta function (0 if $i \neq j$ and 1 if $i = j$). The latter function indicates that the interlayer exchange coupling [see Eq. (2)] is approximated to be active on the next nearest neighbors only. On the other hand, the dynamic components of the effective fields are:

$$h_{x,y}^{e(\nu)} = \sum_\eta \left(d\mu_0 M_s^{(\nu)} M_s^{(\eta)}\right)^{-1} J m_{x,y}^{(\eta)}(\delta_{\nu-1}\delta_\eta + \delta_{\nu+1}\delta_\eta). \tag{7}$$

By inserting Eqs. (6) and (7) into Eqs. (4) and (5), the system can be solved numerically.

Figure 5 shows a direct comparison of FMR experimental data (dots) and theory (lines) evaluated at $\mu_0 H^{\mathrm{OOP}}$ = -1.2 T (saturated regime for any *N*), where the external field is applied normal to the sample. A systematic analysis was performed from the theoretical point of view to reach a good agreement with the FMR data and to justify the use of the proposed model. Typically, FMR is modeled under the assumption that the measured signal is coherent, i.e., the spatial extent of OOP features is small enough that the absorption corresponds to a single average OOP sample structure. By following this line of action, first we use a simple macrospin model to fit the experimental data [see Fig. 5(a)], where each Co layer has the same effective anisotropy field $\mu_0 H_a$

that is set by fitting the frequency of the 1st mode for N=1, while the outer layers have a different effective anisotropy field $\mu_0 H_a^0$ to take into account the effect of having a single neighboring exchange coupled layer.

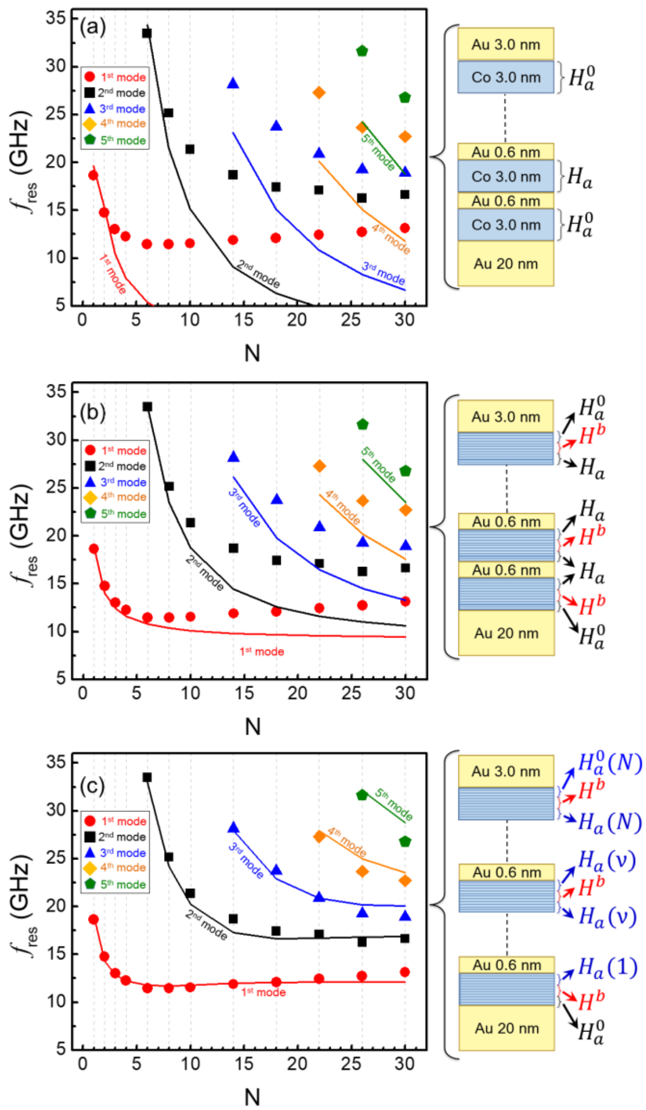

FIG. 5. (a)-(c) FMR measurements (dots) and theory (lines) evaluated at $\mu_0 H$ = -1.2 T. Cases (a)-(c) show different approximations of the theoretical model (see text for details) that are summarized by the layer sketches on the right.

However, attempting to model the FMR data with this simple model results in a truly incorrect fit, as shown in Fig. 5(a). Still, we observe that the model could be useful to explain the behavior of the low-frequency mode (red dots) for the cases of one, two or three Co layers (N = 1, 2, 3) since a reasonable agreement with the experimental results is obtained. Nevertheless, if N increases it is not possible anymore to find a good agreement between the FMR data and the theoretical calculation implying that such a simple macrospin model is not able to capture all the details of the dynamic magnetization for larger N values. Moreover, this first simple approach considers the surface anisotropy fields to be weak within the effective field $\mu_0 H_a$ of the entire 3-nm-thick Co layer in the LL equation of motion, namely they are not assumed as located solely at the Co/Au interfaces.

In order to consider the variations of the dynamic magnetization along the thickness and the interfacially confined nature of the surface anisotropy fields, we use an approach that subdivides the FM layers [54], so that $\boldsymbol{m}^{(\nu)}$ varies along the d = 3 nm thick individual Co layer. Here, we define the anisotropy field $\mu_0 H_a$ uniquely within the sublayers that are next to the Au/Co interfaces, where both magnetocrystalline and surface anisotropy contributions are acting, while within the central region of the FM layer a different bulk anisotropy field parameter ($\mu_0 H^b$) is considered. This latter term originates mainly from the magnetocrystalline anisotropy, which we assume to dominate over the surface anisotropy in the central 3-nm-thick Co film region and is enabled by the crystalline orientation of the ML stack as confirmed by the X-ray characterization and the magnetometry measurements. This case is shown in Fig. 5(b) and the sketch next to it, where we have subdivided each individual FM layer into 12 discrete sublayers with index SL. Twelve SLs is the best compromise between accuracy of the fitting procedure and optimization of the computational time. Thus, sublayers SL = 1 – 4 and 9 – 12 possess an effective field $\mu_0 H_a$, whereas the inner sublayers $5 \leq SL \leq 8$ are dominated by the effective field $\mu_0 H^b$ of magnetocrystalline origin. Once again, the effective fields of the sublayers adjacent to the bottom-most and top-most Co/Au interfaces are represented by a distinct fit parameter $\mu_0 H_a^o$, to account for the distinct boundary conditions. The agreement between the calculations (lines) and the experimental data (symbols) improves in general and substantially for repetition numbers up to N = 6 but fails to reproduce the FMR modes for samples with $N > 6$.

Overall, we noted that for both models the theoretical results always underestimate the experimentally determined FMR frequencies for high N. To account for this effect, we further include a variation of the anisotropy field as a function of the repeating Co film unit within the ML samples, such that the magnetic anisotropy varies as we move from the bottom Co layer (ν = 1) towards the topmost Co layer ($\nu = N$). This type of modeling is challenging, as without significant constraints on the individual magnetic profiles, the number of free parameters can become prohibitively large, rendering the results meaningless. Thus, we have chosen to build the model based on useful information already determined from the previously discussed magnetometry characterization as well as fitting the entire FMR data set with the same set of fitting parameters.

This case is illustrated in Fig. 5(c), where a very good agreement between experiment (symbols) and calculation (straight lines) is finally achieved.

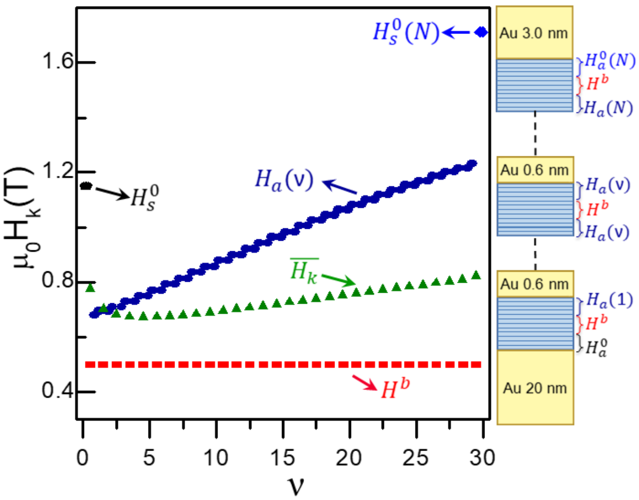

FIG. 6. Anisotropy fields as a function of ν for a sample with N Co/Au bilayers ($1 \leq \nu \leq N$). The bulk (H^b, red squares) as well as the bottom-most and top-most sublayer anisotropy fields (H_a^o, black pentagon and $H_a^o(N)$, light blue rhomb) are assumed fixed, while the anisotropy field at the boundaries of the inner Co layers [$H_a(\nu)$, dark blue dots] increases as its location moves towards the top part of the multilayers stack. The overall average anisotropy fields $\overline{H_K}(\nu)$ are shown as green triangles. The schematics on the right associate each anisotropy field to the corresponding region within the sample.

Figure 6 shows in detail the fitted values for the model depicted in Fig. 5(c). For the inner sublayers of the Co films ($5 \leq SL \leq 8$) the anisotropy field was fixed to $\mu_0 H^b$ = 0.5 T [55], whereas we allowed the interfacial sublayer anisotropy (SL = 1-4, 9-12) to vary from one Co layer to another, as $\mu_0 H_a(\nu)$. In addition, the anisotropy fields of the bottom-most and top-most sublayers adjacent to the Co/Au interfaces are allowed to have different specific values, which were determined from the fit to the N = 1 sample, thus obtaining $\mu_0 H_a^o$ = 1.15 T and $\mu_0 H_a^o(30)$ = 1.70 T, respectively. As can be seen in Fig. 6, the variable anisotropy field $\mu_0 H_a(\nu)$ increases with the Co layer number ν when moving from the bottom part of the ML stack upwards, while its slope becomes smaller with increasing ν. If we consider the obtained anisotropy values for $10 \leq \nu \leq 30$, we nicely find that the average value of the total uniaxial anisotropy field is $\mu_0 \overline{\overline{H_k}}$ = 0.75 ± 0.04 T, in good agreement with $2K_u/\mu_0 M_s$ = 0.73 T that was evaluated from VSM data using the simple model of Fig. 3(o) and Eq. (1).

The vertical gradient in the anisotropy field term $\mu_0 H_a(\nu)$, is explained in terms of the growth induced strain relaxation process we had found when analyzing the XRD data [56,57]. As subsequent Co/Au bilayers are grown, the introduction of misfit dislocations relieves the stress accumulated due to the mismatch of the Co/Au stack with the Au(111) buffer layer. It is also natural to assume that as more Co/Au bilayers are grown, the stress that builds up gradually attenuates. In fact, we found that most of the strain relaxation occurs upon growth of the first ten Co/Au bilayers [see Fig. 2(b)]. Thus, the density of the aforementioned misfit dislocations would naturally decrease when going from the Co/Au interfaces located in the bottom part of the ML stack towards the top-most interfaces.

It has been reported that misfit dislocations at interfaces in *hcp* Co films often consist of *fcc*-like inclusions, thus locally impacting the magnetocrystalline anisotropy energy of Co films due to the lower anisotropy of the *fcc*-like ordering as compared to *hcp* [58-60]. Thus, we can now connect the gradient in the magnetic anisotropy field obtained from the fit to the dynamic model with a gradient in the concentration of misfit dislocations at the Co/Au interfaces. In the bottom region of the multilayer stack, a larger number of dislocations appears due to the larger stress build-up, which then effectively lowers the magnetocrystalline anisotropy contribution to the $\mu_0 H_a(\nu)$ term. As growth progresses and strain is gradually released, fewer dislocations are introduced, and thus, the magnetocrystalline anisotropy term to $\mu_0 H_a(\nu)$ being less affected by the presence of fcc-like inclusions in the interfacial region, such that a larger magnetic anisotropy develops towards the top region of the Co/Au ML stack.

It is interesting to consider that a variation of the $\mu_0 H_a(\nu)$ along the vertical direction of the ML stack could also originate from a different surface anisotropy contribution as we go from one Co/Au interface to another along the vertical direction. In fact, the surface waviness observed in the TEM micrograph in Fig. 2(c) might suggest that the surface anisotropy is influenced by the non-ideal, wavy interface geometry. TEM imaging does not show, however, a clear gradient of the waviness when moving from the bottom-most to the top-most part of the stacks, such that we associate the main contribution to the anisotropy field gradient from a perspective of strain relaxation induced magnetocrystalline anisotropy reduction by the presence of dislocations.

The proposed model also allows for evaluating the depth profile of the dynamic response amplitude. The corresponding dynamic magnetization profiles are shown in Fig. 7. In Fig. 7(a) the case of one isolated FM layer (N =1) is shown where the orbits of the sublayers are depicted. The red dots denote the t = 0 point, i.e., they mark the excitation amplitude and phase for all modes at the same time, while the orbit highlighted with yellow thick dots corresponds to the orbit of the 7-th sublayer. As the number of layers increases, the orbits change radically as depicted in Figs. 7(b)-(d), introducing an amplitude distribution throughout the layers while keeping them in phase. Due to the different anisotropies at the top and bottom parts of the ML, the higher amplitude is mainly located at the bottom part of the structure, where the local anisotropies are smaller. This behavior explains why the first mode (or low-frequency mode) does not significantly change at higher values of N. Indeed, by increasing N the first mode becomes gradually a mode that is confined at the bottom part of the sample. The excited mode profiles for N = 30 are illustrated in Figs. 7(e)–(f), which are showing the nonmonotonic amplitude profiles of the high order modes, whose distribution depends on the energy profile along the total thickness.

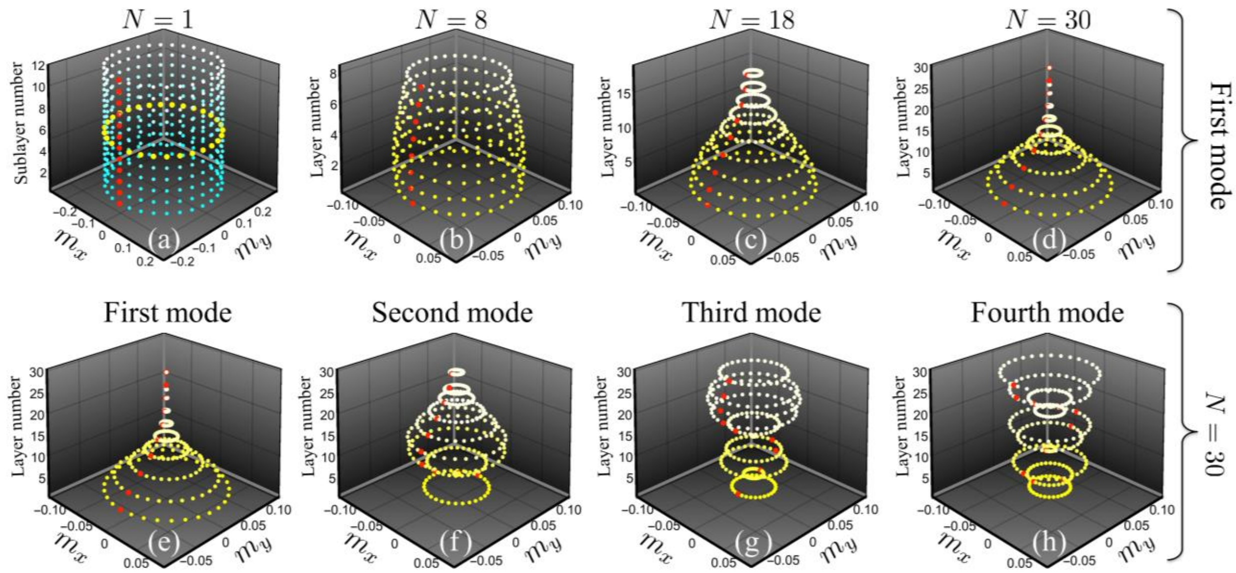

FIG. 7. In-plane dynamic magnetization orbits in z-direction across the sample thickness as a function of N. In cases (a)–(d) the first mode is illustrated for different N values, while the first four excited modes are shown in (e)–(h) for the case N=30. Dynamic magnetization components $m_{x,y}$ are expressed in arbitrary units. The rod dots mark the excitation amplitude and phase for all modes at the same time (t=0).

For high mode numbers the phase changes by 180°, giving them a spin wave character. Therefore, a PSSW-like mode in thinner ML films needs dramatically more energy, due to higher exchange energy needed for the same kind of wave.

IV. Conclusions

In this paper, we have successfully fabricated [Co(3.0 nm)/Au(0.6 nm)]$_N$ multilayer films with a magnetic anisotropy axis perpendicular to the ML plane. The RT magnetometry measurements for the samples with N > 10 reveal two very different magnetization reversal processes for external applied fields within and perpendicular to the film plane: namely (i) an instability-driven reversal process leading to the generation of parallel stripe domains for IP field orientation and (ii) a domain nucleation process that is hysteretic in nature for OOP field orientation [30]. Our N-dependent study shows a gradual shrinking of the nucleation regime with decreasing N, so that at sufficiently low N only the instability-driven second-order phase transition occurs even for OOP applied fields.

The disappearance of the nucleation regime is driven by the strongly thickness-dependent balance between magnetic anisotropy and magnetostatic energies and occurs before the effective OOP anisotropy energy becomes too weak to support a stripe domain state altogether, i.e., it occurs while the stripe domain instability is still dominating the magnetization reversal process by spontaneously forming stripe domains at a critical applied field without a real bubble nucleation and stripe propagation process. By further reducing the number of Co/Au repetitions below N<10, we observe a characteristic in-plane easy-plane magnetic behavior.

Moreover, we have demonstrated that such MLs provide an efficient platform for the excitation of PSSWs, whose characteristics turns out to be strongly dependent on the material modulation along the total thickness induced by the multilayering itself. Specifically, we identify various dynamic excitations for statically OOP saturated multilayer state, which are excited under rf fields. Therefore, in contrast to homogeneous thick films or thin multilayer systems, the investigated structures allow for a full comprehension of the conversion of periodic material and magnetic properties along the sample stack into a vertical array of two-dimensional (exchange-based) pinning sites for the PSSW modes within the film. In this context, in particular the decreased exchange across the Au interlayers seems to be responsible for the more complex dynamic behavior, as compared to systems with a less strong vertical exchange modulation, such as for example in typically investigated Co/Pt and Co/Pd ML systems. Moreover, we demonstrate that PSSW modes provide a handle to study the magnetic interactions and their modulation along the thickness in such ML systems, offering a unique platform for full tunability of the mode frequencies and amplitude profiles. Our observations can be generalized for different multilayered ferromagnetic materials exhibiting OOP preferential orientation of magnetization. Overall our work illustrates the substantial relevance of PMA thin films for a very detailed understanding of high-frequency spin wave excitations in artificially multilayered systems.

ACKNOWLEDGMENTS

L. F. is very thankful to K. Potzger for the support with experimental facilities. R. A. G. acknowledges the financial support from Fondecyt Iniciación, Grant 11170736 and Basal Program for Centers of Excellence, Grant FB0807 CEDENNA, CONICYT. CzechNanoLab project LM2018110 funded by MEYS CR is gratefully acknowledged for supporting the experimental work at CEITEC Nano Research Infrastructure. This work has received funding from the European Union's Horizon 2020 research and innovation program under the Marie Skłodowska-Curie Actions and it is co-financed by the South Moravian Region under grant agreement No. 665860. The use of the HZDR Ion Beam Center TEM facilities is gratefully acknowledged.

References

[1] M. N. Baibich, J. M. Broto, A. Fert, F. Nguyen Van Dau, F. Petroff, P. Etienne, G. Creuzet, A. Friederich, and J. Chazelas, Phys. Rev. Lett. **61**, 2472 (1988).

[2] P. M. Levy, S. Zhang, and A. Fert, Phys. Rev. Lett. **65**, 1643 (1990).

[3] M. T. Johnson, P. J. H. Bloemen, F. J. A. den Broeder, and J. J. de Vries, Rep. Prog. Phys. **59**, 1409 (1996).

[4] P. F. Carcia, A. D, Meinhaldt, and A. Suna, Appl. Phys. Lett. **47**, 178 (1985).

[5] W. B. Zeper, F. J. A. M. Greidanus. P. F. Carcia and C. R. Fincher, J. of Appl. Phys. **65**, 4971 (1989).

[6] C. J. Lin, G. L. Gorman, C. H. Lee, R. F. C. Farrow, E. E. Marinero, H. V. Do, H. Notarys, C. J. Chien, J. Magn. Magn. Mater. **93**, 194 (1991).

[7] D. Weller, W. Reim, K. Spörl, and H. Brändle, J. Magn. Magn. Mater. **93**, 183 (1991).

[8] O. Hellwig, A. Berger, J. B. Kortright, and E. E. Fullerton, J. Magn. Magn. Mat. **319**, 13-55 (2004).

[9] J. E. Davies, O. Hellwig, E. E. Fullerton, G. Denbeaux, J. B. Kortright, and K. Liu, Phys. Rev. B **70**, 224434 (2004).

[10] R. Sbiaa, Z. Bilin, M. Ranjbar, H. K. Tan, S. J. Wong, S. N. Piramanayagam, and T. C. Chong, J. Appl. Phys. **107**, 103901 (2010).

[11] C. Kittel, Rev. Mod. Phys. **21**, 541-583 (1949); C. Kittel and J. K. Galt, Solid State Phys. **3**, 437-565 (1956).

[12] A. Hubert and R. Schäfer, Magnetic Domains (Springer-Verlag Berlin Heidelberg, 1998).

[13] S. S. P. Parkin, H. Hopster, J- P. Renard, T. Shinjo, and W. Zinn Magnetic Surfaces, Thin Films, and Multilayers, MRS Symposia Proceedings No. 231 (Materials Research Society, Pittsburgh, 1992).

[14] M. Hehn, S. Padovani, K. Ounadjela, and J. P. Bucher, Phys. Rev. B **54**, 3428 (1996).

[15] E. Sallica Leva, R. C. Valente, F. Martínez Tabares, M. Vásquez Mansilla, S. Roshdestwensky, and A. Butera, Phys. Rev. B **82**, 144410 (2010).

[16] L. Fallarino, O. Hovorka, and A. Berger, Phys. Rev. B **94**, 064408 (2016).

[17] T. G. Phillips and H. M. Rosenberg, Rep. Prog. Phys. **29**, 285 (1966).

[18] S. E. Barnes, Adv. Phys. **30**, 801 (1981).

[19] Z. Frait and D. Fraitova, Spin Waves and Magnetic Excitations, edited by A. S. Borovik-Romanov and S. K. Sinha (Elsevier, Amsterdam, 1988, Vol. 2).

[20] B. Heinrich and J. F. Cochran, Adv. Phys. **42**, 523 (1993).

[21] Z. Celinski, K. B. Urquhart, and B. Heinrich, J. Magn. Magn. Mater. **166**, 6 (1997).

[22] M. Farle, Rep. Prog. Phys. **61**, 755 (1998).

[23] G. Srinivasan and A. N. Slavin, High Frequency Processes in Magnetic Materials (World Scientific, River Edge, New Jersey ,1994); P. E. Wigen, Thin Solid Films **114**, 135 (1984); C. E. Patton, Phys. Rep.**103**, 251 (1984).

[24] Y. V. Khivintsev, L. Reisman, J. Lovejoy, R. Adam, C. M. Schneider, R. E. Camley, and Z. J. Celinski, J. Appl. Phys. **108**, 023907 (2010).

[25] K. J. Kennewell, M. Kostylev, N. Ross, R. Magaraggia, R. L. Stamps, M. Ali, A. A. Stashkevich, D. Greig, and B. J. Hickey, J. Appl. Phys. **108**, 073917 (2010).

[26] M. A. W. Schoen, J. M. Shaw, H. T. Nembach, M. Weiler, and T. J. Silva, Phys. Rev. B **92**, 184417 (2015).

[27] H. Qin, S. J. Hämäläinen, and S. van Dijken, Sci. Rep. **8**, 5755 (2018).

[28] A. Navabi, C. Chen, A. Barra, M. Yazdani, G. Yu, M. Montazeri, M. Aldosary, J. Li, K. Wong, Q. Hu, J. Shi, G. P. Carman, A. E. Sepulveda, P. Khalili Amiri, and K. L. Wang, Phys. Rev. Applied **7**, 034027 (2017).

[29] Z. Chen, Y. Yan, S. Li, X. Xu, Y. Jiang, and T. Lai, Sci. Rep. **7**, 42513 (2017).

[30] L. Fallarino, A. Oelschlägel, J. A. Arregi, A. Bashkatov, F. Samad, B. Böhm, K. Chesnel, and O. Hellwig, Phys. Rev. B **99**, 024431 (2019).

[31] M. Lakshmanan, Phil. Trans. R. Soc. A **369**, 1280 (2011).

[32] W. Jiang, G. Chen, K. Liu, J. Zang, S. G. E. te Velthuis, and A. Hoffmann, Phys. Rep. **704**, 1 (2017).

[33] M. Langer, K. Wagner, T. Sebastian, R. Hübner, J. Grenzer, Yutian Wnag, T. Kubota, T. Schneider, S. Stienen, K. Lenz, H. Schultheiß, J. Lindner, K. Takanashi, R. E. Arias, J. Fassbender, Appl. Phys. Lett **108**, 102402 (2016).

[34] L. Fallarino, V. Sluka, B. Kardasz, M. Pinarbasi, A. Berger, and A. D. Kent, Appl. Phys. Lett. **109**, 082401 (2016).

[35] Here, the value $t_{\mathrm{Co/Au}}$ refers to two independent averaging processes: one is directly connected to the volume averaged nature of the x-ray measurements, which indeed depends on the penetration depth of the beam as well as on its lateral extension; the second one is the arithmetic mean of the thicknesses calculated via the angular position of the first, second and third order Bragg-like superstructure peaks at low angles.

[36] Despite our XRD investigation not being able to exclude the presence of *fcc* stacking faults in Co, the *hcp* lattice of Co was additionally verified via in-plane diffraction measurements, by setting the incident and diffracted beams nearly parallel to the sample surface, in which only Co($11\bar{2}0$), Co($10\bar{1}0$) and Au(220) reflections were measured for our samples. The in-plane diffraction experiments confirmed a fiber-textured ordering of the multilayers, with randomly in-plane oriented crystallographic planes.

[37] Zs. Czigány and G. Radnóczi, Thin Solid Films **347**, 133-145 (1999).

[38] M. A. Monclús, M. Karlik, M. Callisti, E. Frutos, J. LLorca, T. Polcar, J. M. Molina-Aldareguía, Thin Solid Films **571**, 275-282 (2014).

[39] R. L. Stamps and B. Hillebrands, Phys. Rev. B **43**, 3532 (1991).

[40] A. Kashuba, V. L. Pokrovsky, Phys. Rev. Lett. **70**, 3155 (1993).

[41] A. Berger, H. Hopster, J. Appl. Phys. **79**, 5619 (1996).

[42] D. M. Donnet, K. M. Krishnan, and A. Yajima, J. Phys. D **28**, 1942 (1996).

[43] C. Kooy and U. Enz, Philips Res. Rep. **15**, 7 (1960).

[44] N. Saito, H. Fujiwara, and Y. Sugita, J. Phys. Soc. Jpn. **19**, 1116 (1964).

[45] J. Muller, J. Appl. Phys. **38**, 2413 (1967).

[46] Y. Murayama, J. Phys. Soc. Jpn. **21**, 2253 (1966).

[47] B. Kaplan and G. A. Gehring, J. Magn. Magn. Mat. **128**, 111 (1993).

[48] G. Bertotti, Hysteresis in Magnetism (Academic Press, San Diego, 1998).

[49] F. Wilhelm, M. Angelakeris, N. Jaouen, P. Poulopoulos, E. Th. Papaioannou, Ch. Mueller, P. Fumagalli, A. Rogalev, and N. K. Flevaris, Phys. Rev. B **69**, 220404(R) (2004).

[50] P. Bruno, J. Magn. Magn. Mater. **121**, 238 (1993).

[51] S. M. Rezende, C. Chesman, M. A. Lucena, A. Azevedo, and F. M. de Aguiar, J. Appl. Phys. **84**, 958 (1998).

[52] T. Kingetsu and K. Sakai, Phys. Rev. B **48**, 4140 (1993).

[53] H. Fritzsche, J. Kohlhepp, and U. Gradmann, J. Magn. Magn. Mat. **148**, 154-155 (1995).

[54] V. Sluka, T. Schneider, R. A. Gallardo, A. Kákay, M. Weigand, T. Warnatz, R. Mattheis, A. Roldán- Molina, P. Landeros, V. Tiberkevich, A. Slavin, G.Schütz, A. Erbe, A. Deac, J. Lindner, J. Raabe, J. Fassbender, and S. Wintz, Nat. Nanotechnol. **14**, 328 (2019).

[55] K. Chesnel, A. S. Westover, C. Richards, B. Newbold, M. Healey, L. Hindman, B. Dodson, K. Cardon, D. Montealegre, J. Metzner, T. Schneider, B. Böhm, F. Samad, L. Fallarino, and O. Hellwig, Phys. Rev. B **98**, 224404 (2018).

[56] L. Reichel, G. Giannopoulos, S. Kauffmann-Weiss, M. Hoffmann, D. Pohl, A. Edström, S. Oswald, D. Niarchos, J. Rusz, L. Schultz, and S. Fähler, J. Appl. Phys. **116**, 213901 (2014).

[57] J. A. Arregi, J. B. González-Díaz, O. Idigoras, and A. Berger, Phys. Rev. B **92**, 184405 (2015).

[58] C. K. Lo, Y. Liou, C. P. Chang, I. Klik, and Y. D. Yao, and J. C. A. Huang, Appl. Phys. Lett. **68**, 2155 (1996).

[59] W. Yang, D. N. Lambeth, and D. E. Laughlin, J. Appl. Phys. **87**, 6884 (2000).

[60] V. Sokalski, D. E. Laughlin, and J.-G. Zhu, J. Appl. Phys. **110**, 093919 (2011).